Single-Atom Catalysis

CO-Induced Dimer Decay Responsible for Gem-Dicarbonyl Formation on a Model Single-Atom Catalyst

Chunlei Wang[+], Panukorn Sombut[+], Lena Puntscher, Zdenek Jakub, Matthias Meier, Jiri Pavelec, Roland Bliem, Michael Schmid, Ulrike Diebold, Cesare Franchini, and Gareth S. Parkinson*

Abstract: The ability to coordinate multiple reactants at the same active site is important for the wide-spread applicability of single-atom catalysis. Model catalysts are ideal to investigate the link between active site geometry and reactant binding, because the structure of single-crystal surfaces can be precisely determined, the adsorbates imaged by scanning tunneling microscopy (STM), and direct comparisons made to density functional theory. In this study, we follow the evolution of Rh_1 adatoms and minority Rh_2 dimers on $Fe_3O_4(001)$ during exposure to CO using time-lapse STM at room temperature. CO adsorption at Rh_1 sites results exclusively in stable Rh_1CO monocarbonyls, because the Rh atom adapts its coordination to create a stable pseudo-square planar environment. $Rh_1(CO)_2$ gem-dicarbonyl species are also observed, but these form exclusively through the breakup of Rh_2 dimers via an unstable $Rh_2(CO)_3$ intermediate. Overall, our results illustrate how minority species invisible to area-averaging spectra can play an important role in catalytic systems, and show that the decomposition of dimers or small clusters can be an avenue to produce reactive, metastable configurations in single-atom catalysis.

Introduction

So-called "single-atom catalysts" (SACs) have attracted much attention in recent years due to their reported catalytic performance and high atomic utilization.[1] However, significant controversy remains regarding whether single atoms are the primary catalytic active sites, even for simple reactions like CO oxidation. Some argue that single atoms are indeed the catalytic centers, and invoke a Mars–van Krevelen mechanism.[2] In this scenario, the primary role of the metal atom is to strongly bind the CO in close proximity to the support to facilitate a reaction with lattice oxygen. Other studies suggest that simultaneous coordination of CO and O_2 can occur at the same adatom site, but this depends strongly on the metal and support in question, and local coordination environment.[3] Finally, other studies suggest that single atoms are inert and/or unstable,[4] and that larger clusters are responsible for the observed activity.[5]

In recent years, it has been suggested that SACs could be used to heterogenize reactions typically performed by mononuclear complexes in homogeneous catalysis. Alkene hydroformylation has been demonstrated for Rh_1 species on various metal oxide supports,[6] with activity and selectivity for aldehydes rivalling that of the Rh_1 complexes used in industry. Theoretical calculations suggest that the reaction proceeds in much the same way as in the homogeneous system,[6c,d] via simultaneous coordination of CO, alkene, and H at the same metal center. Assuming the analogy holds true, attaching multiple ligands requires a Rh atom with a low coordination on the oxide support, which is typically an unstable situation.

Understanding how the local binding environment of a metal atom affects adsorption is desirable, but difficult to achieve for high-surface-area catalyst supports. Scanning transmission electron microscopy (STEM) is typically used to image such systems, but this technique is insensitive to elements with low atomic mass. The oxygen atoms of the support lattice are thus not imaged, and in any case, STEM

[*] C. Wang,[+] P. Sombut,[+] L. Puntscher, Z. Jakub, M. Meier, J. Pavelec, M. Schmid, U. Diebold, G. S. Parkinson
Institute of Applied Physics, TU Wien, Vienna, 1040, Austria
E-mail: gareth.parkinson@tuwien.ac.at

Z. Jakub
Central European Institute of Technology (CEITEC), Brno University of Technology, Brno, 612 00, Czechia

M. Meier, C. Franchini
Faculty of Physics, Center for Computational Materials Science, University of Vienna,
Vienna, 1090, Austria

C. Franchini
Dipartimento di Fisica e Astronomia, Università di Bologna, Bologna, 40127, Italy

R. Bliem
Advanced Research Center for Nanolithography,
1098XG Amsterdam, Netherlands

[+] These authors contributed equally to this work

produces a 2-dimensional representation of a 3-dimensional object so local coordination information is difficult to ascertain. Most SAC studies utilize extended X-ray absorption fine structure (EXAFS) to shed light on the metal coordination, but this technique provides area-averaged information (not necessarily that of the active site) and conclusions are usually made by comparison to bulk reference samples. The coordination will be different for a surface adatom, and in a reactive environment the impact of adsorbed molecules (e.g., water, hydroxyl groups, reactant species) on EXAFS spectra is not clear. As such, the link between experiment and theory is tenuous, and there is a need to better understand how the local coordination environment affects the adsorption of reactants in SAC.

In this paper, we study Rh species on a single crystal $Fe_3O_4(001)$ support, where the support structure and active site geometry is precisely known. Combining time-lapse scanning tunneling microscopy (STM) and density functional theory calculations (DFT), we follow the adsorption of CO at room temperature and determine how molecules adsorb. The data reveal that CO adsorption at Rh_1 species leads exclusively to monocarbonyls, whose stability is enhanced by an adaptation of the Rh coordination to the support. $Rh_1(CO)_2$ dicarbonyls (named geminal or gem-dicarbonyls) are also observed, but these form exclusively via the break-up of Rh_2 dimers through an unstable $Rh_2(CO)_3$ intermediate. Our results reveal how Rh atoms adapt their environment in the presence of reactant molecules, and that decomposition of metastable dimers and small clusters can be a conduit to produce "single-atom" sites capable of accommodating multiple ligands.

Results and Discussion

The $Fe_3O_4(001)$ support utilized in this work exhibits a $(\sqrt{2}\times\sqrt{2})R45°$ periodicity due to an ordered array of subsurface cation vacancies and interstitials.[7] STM images of the as-prepared surface (Figure S1) exhibits rows of protrusions attributable to the surface Fe atoms. These atoms are 5-fold coordinated to lattice oxygen, as established previously.[7] The oxygen atoms are not visible in STM images because they have little density of states near the Fermi level, but their positions are confirmed by quantitative low-energy electron diffraction[7] and surface x-ray diffraction[8] experiments. Evaporation of 0.2 ML Rh onto the surface in ultrahigh vacuum (UHV) at room temperature results in bright protrusions located midway between the Fe rows (indicated by yellow arrows in Figure 1a).[9] These are Rh_1 adatoms. The position within the unit cell is essentially where the next tetrahedrally coordinated Fe cation would reside if the bulk structure were continued outwards, which is consistent with several other metals studied previously.[7,9a,10] Figure 1b shows the same sample area after adsorption of 17 L CO at room temperature. The Rh_1 adatoms appear elongated in STM following CO adsorption along the direction of the surface Fe rows.

The remainder of Figure 1 shows computational results for the $CO/Rh_1/Fe_3O_4(001)$ system. Figure 1c shows the

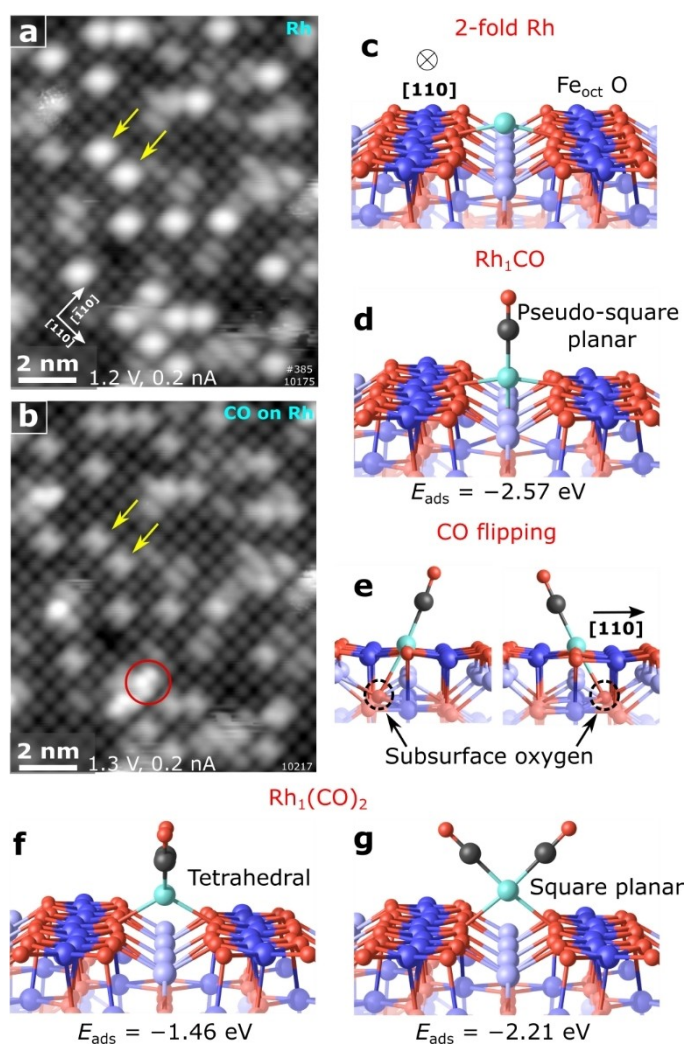**Figure 1.** CO adsorption on 2-fold coordinated $Rh_1/Fe_3O_4(001)$. (a–b) STM images of 0.2 ML Rh on $Fe_3O_4(001)$ surface before (a) and after (b) exposure to 17 L CO. The yellow arrows mark the Rh adatoms located between the rows of surface Fe atoms. The red circle highlights a Rh_1 gem-dicarbonyl. (c) Perspective view model of a Rh_1 adatom (cyan) adsorbed on the $Fe_3O_4(001)$-$(\sqrt{2}\times\sqrt{2})R45°$ surface. Surface Fe_{oct} atoms are dark blue, tetrahedrally coordinated Fe_{tet} atoms are lighter and slate blue. Oxygen, carbon, and Rh_1 atoms are red, black, and cyan, respectively. (d) CO adsorption induces a downward relaxation of the Rh, which achieves a pseudo-square planar bonding environment via a weak bond to a subsurface O atom. (e) Side view of the Rh_1 monocarbonyl in (d). The orientation of the CO can flip between two symmetrically equivalent positions due to the presence of two equivalent O atoms in the subsurface layer (indicated by the black dashed circles). (f–g) Rh gem-dicarbonyl with tetrahedral (f) and square-planar (g) orientation of the CO molecules. E_{ads} is the average adsorption energy per CO molecule.

optimal configuration of the Rh_1 adatom (cyan). It is located in the high-symmetry position midway between the surface iron rows (dark blue) and 2-fold coordinated to surface oxygen atoms (red). It protrudes 0.72 Å above the plane of the surface Fe atoms, and has an adsorption energy of -4.57 eV referenced to a gas-phase Rh atom. The Bader charge of $+0.71\,e$ is consistent with a cationic charge state of

+1, and typical for metal atoms on Fe_3O_4(001).[9a] Figure 1d shows the configuration obtained after adsorption of a single CO molecule. The CO coordinates to the Rh atom, which sinks down towards the surface and forms a weak bond to a subsurface O atom (bond length = 2.27 Å). This creates a pseudo-square planar environment for the Rh atom, which again exhibits a Bader charge of +0.71 e. This is consistent with the +1 oxidation state expected for square-planar d^8 complexes. Since the subsurface O is not directly beneath the Rh site, the CO is tilted away from the surface normal. Because there are two symmetrically equivalent subsurface oxygen atoms, there are two symmetrically equivalent configurations, as shown in the side view of Figure 1e. The two configurations lead to the CO flipping (a movie illustrating this flipping motion is included as Movie S1). The barrier to flip between the configurations is determined computationally to be ≈ 0.1 eV, which means that the flipping will be rapid at room temperature. The STM measurement is slow in comparison, and the elongated protrusion imaged in Figure 1b is thus a superposition of the two states.

An alternative explanation for the elongated protrusions observed on Figure 1b could be the adsorption of 2 CO molecules oriented along the Fe row direction as the calculated model in Figure 1f. However, this gem-dicarbonyl geometry creates a tetrahedral coordination for the Rh atom, which is highly unfavorable (−1.46 eV per CO) compared to a square planar configuration formed by adsorbing two CO molecules oriented perpendicular to the Fe row direction as shown in Figure 1g (−2.21 eV per CO). The Bader charge (+0.69 e) of the Rh atom is again consistent with an oxidation state of +1, which would be expected for a Rh atom in a square planar d^8 complex. Thus, the extent of the charge transfer between adatom and support is governed by the coordination environment of the Rh atom. A similar conclusion was reached in a recent STM study of the Ir/Fe_3O_4(001) system.[11] A full comparison of Bader charges and magnetic moments of the different Rh_1 configurations is given in Table S1. The strong adsorption energy of the gem-dicarbonyl suggests it should be stable at room temperature. The red circle in Figure 1b shows an example of a protrusion with the expected appearance of such a Rh gem-dicarbonyl i.e., two bright lobes located above two opposite Fe rows. We observed similar features in our recent STM study of the Ir/Fe_3O_4(001) system, and assigned them as gem-dicarbonyl species.[11] However, the coverage was always less than 10% of the Ir-related features. This behavior is replicated here for Rh: The coverage of $Rh_1(CO)_2$ species saturates at $\approx 5\%$ of Rh species at 0.14 ML coverage after an exposure to CO at room temperature.

To study how the observed Rh_1 gem-dicarbonyls form, we imaged the Rh/Fe_3O_4(001) sample by STM during exposure to CO at 10^{-9} mbar (Supplementary Movie S2). Over the course of the movie all the Rh_1 species adsorbed a CO molecule, and took on the appearance of the Rh_1CO shown in Figure 1b (yellow arrows). Direct conversion from Rh_1CO to $Rh_1(CO)_2$ was never observed. In what follows,

we will demonstrate that $Rh_1(CO)_2$ species form via the CO-induced break-up of Rh_2 species.

First, we will introduce the bare Rh_2 dimers, which form spontaneously during Rh deposition. Figures 2(a–b) show two selected frames from an STM movie of a 0.2 ML Rh/Fe_3O_4(001) acquired in UHV at room temperature. The cyan arrows indicate slightly larger oval shaped features that we have previously identified as Rh_2 dimers on the basis that they split into two Rh_1 atoms when scanned at high bias (>3 V) with the STM.[9b] In STM movie frames shown in Figure 2, the dimers exhibit a characteristic motion about the high-symmetry position usually occupied by an adatom. The white dashed lines shown in Figure 2(a,b) pass through Rh_1 adatoms (indicated by yellow arrows), which are located at the high-symmetry position and immobile during the course of the movie. The three Rh_2 dimers flip such that one Rh atom remains on the white dashed line, with the second offset to either side. This behavior is explained by the minimum-energy configuration determined by our DFT calculations, which show that the Rh_2 dimer has one atom in an adatom-like configuration at the high symmetry position of the $(\sqrt{2} \times \sqrt{2})$R45° unit cell (pink arrow in Figure 2c), while the second Rh atom is displaced (blue arrow in
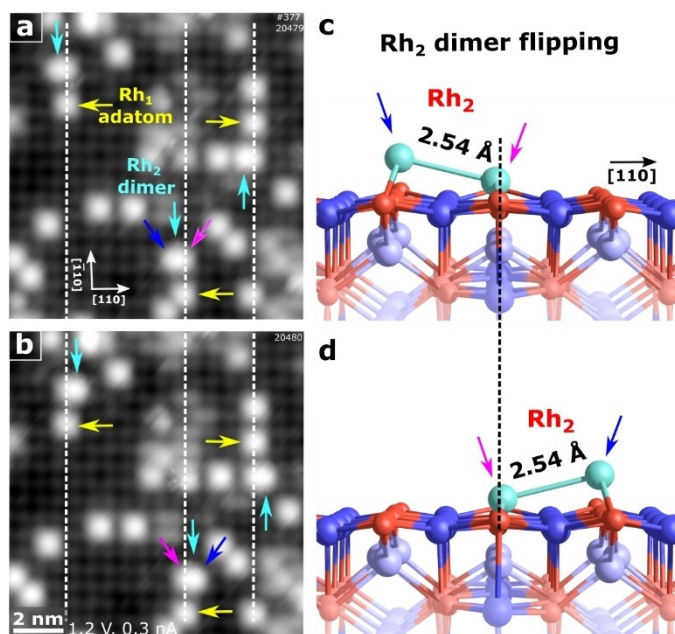

Figure 2. Structure and behavior of Rh dimers on Fe_3O_4(001). (a–b) Two frames of a STM movie show the Rh_2 dimer flipping between two symmetrically equivalent configurations between the surface Fe rows. The yellow arrows each indicate an immobile 2-fold coordinated Rh_1 atom, which is used as a reference. The Rh_2 dimers are marked by cyan arrows. The dashed white lines indicate the same position in the two frames of the STM movie. (c–d) Side view of the Rh_2 dimer. The lower atom (pink arrow) of the Rh_2 dimer is 2-fold coordinated to surface oxygen in the high-symmetry position of the unit cell, and we thus refer to it as "adatom-like". The higher Rh atom (blue arrow) is displaced along the direction of the surface Fe rows, and we refer to it as "displaced". The side view structural models illustrate the two symmetrically equivalent configurations that cause the flipping seen in STM at room temperature (pink and blue arrows).

Figure 2c) along the direction of the Fe rows with a Rh–Rh distance of 2.54 Å. The displaced Rh atom is physically higher than the adatom-like Rh atom due to the presence of tetrahedral Fe below its site. The Rh dimer is more stable than two isolated Rh adatoms by 0.19 eV. The flipping motion observed in the STM movies occurs because there are two symmetrically equivalent positions for the dimer (Figure 2c,d). CI-NEB calculations suggest the barrier to switch between these two states is ≈ 0.90 eV, consistent with the slow motion of the dimer observed in the room temperature STM movie. An animation showing the DFT-determined minimum-energy pathway is included as Movie S3. Other possible Rh_2 dimer configurations were also investigated and found to be less stable. These are shown in Figure S2.

Figure 3 shows three frames selected from an STM movie (Movie S2) acquired from a sample with 0.2 ML Rh deposited on $Fe_3O_4(001)$, and a total exposure of 17 L CO. At this coverage, approximately 12% of the Rh is contained within dimers. In the initial state (Figure 3a) two Rh_2 dimers are highlighted by dashed cyan circles. In Figure 3b, both Rh_2 exhibit a similar appearance with an increased apparent height of ≈ 100 pm following the adsorption of CO. At the end of the movie, both Rh_2 dimers are replaced by one Rh_1CO and one feature identified as $Rh_1(CO)_2$ in Figure 1. It is important to note that an STM tip effect is excluded in our work because the same features are detected after CO adsorption in areas where time-lapse STM was not performed (see Figure S3).

To understand how the breakup of the Rh_2 dimers occurs, we performed DFT calculations. A systematic approach was employed to determine the lowest-energy configuration for 1 CO, 2 CO and 3 CO molecules adsorbed at the Rh_2 dimer. For one CO molecule, the CO can be adsorbed at either of the two Rh atoms. In the most favorable configuration (see Figure 3d), the CO is adsorbed at the displaced Rh, with an adsorption energy of -2.42 eV. The displaced Rh atom tilts slightly towards one side along the Fe_{oct} row, but the Rh–Rh bond length remains 2.48 Å, which is even shorter than the bare Rh dimer. Moving the CO molecule to the adatom-like Rh atom costs 0.35 eV. Further details and alternative configurations are shown in Figure S4.

In principle, the addition of a second CO molecule can occur in three ways. Either both CO molecules are hosted at one of the Rh atoms, or one is adsorbed at each. The CO adsorption energies on each configuration determined by DFT calculations are shown in Figure S5. The most favorable configuration has the Rh atoms straddling the high-symmetry site, bound to two surface O atoms on opposite rows (Figures 3e and S5a), and has a Rh–Rh bond length of 2.49 Å. In this state, it is possible for the $Rh_2(CO)_2$ to adsorb a third CO molecule in the bridge adsorption site between the two Rh atoms (Figure 3f and Figure S6a). This results in an elongation of the Rh–Rh bond length to 2.72 Å, but this in itself does not directly induce the split. In what follows, we describe the proposed splitting process on the basis of Figure 4 and Movie S4.
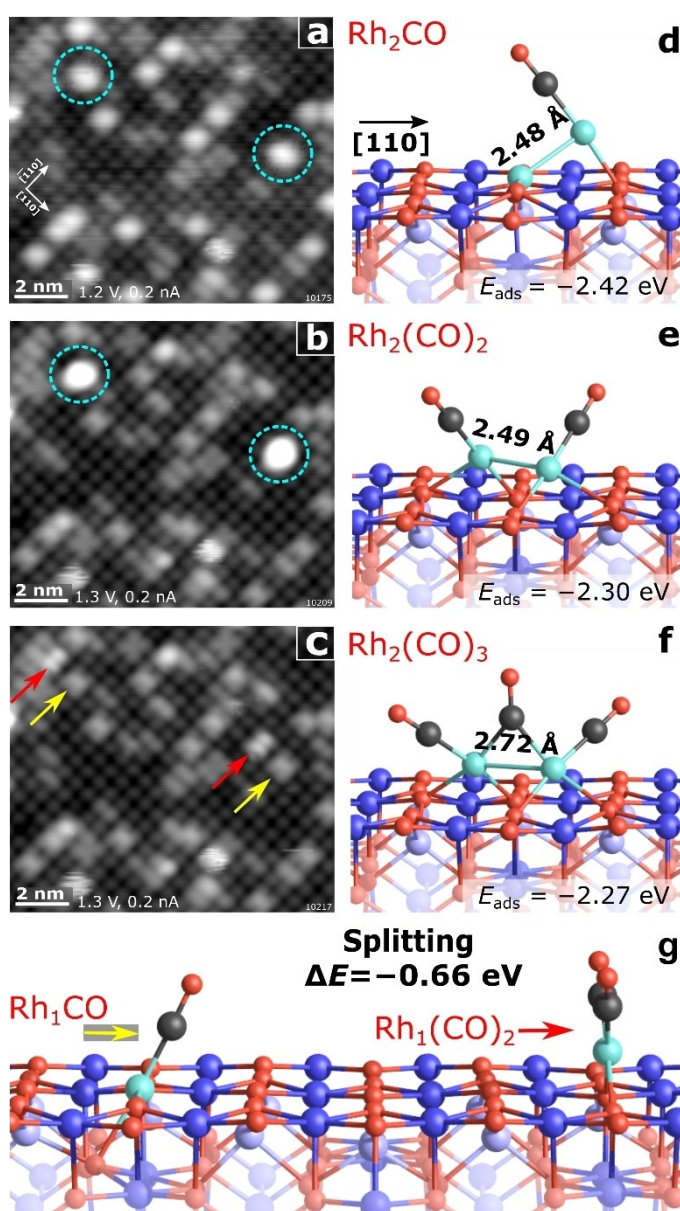

Figure 3. CO-induced breakup of the Rh_2 dimers. (a–c) Three selected frames from Movie S2 that illustrate the sequential adsorption of CO on two Rh_2 species (a, dashed cyan circle). In total, 17 L CO was introduced into the UHV chamber during the course of the experiment. (b) Both highlighted Rh_2 species adsorb CO and form $Rh_2(CO)_x$ species. (c) A short time later, the $Rh_2(CO)_3$ split to form a Rh_1CO (yellow arrow) and a $Rh_1(CO)_2$ gem-dicarbonyl (red arrow) in two adjacent unit cells. (d–f) Minimum-energy configuration for 1, 2 and 3 CO molecules adsorbed at the Rh_2 as determined by DFT. The Rh–Rh bond length increases with the addition of each CO molecules until $Rh_2(CO)_3$, where the Rh–Rh distance is 2.72 Å. (g) The adsorption of 3 CO molecules will finally induce the dimer breakup to a Rh_1CO and a $Rh_1(CO)_2$ as indicated in (c). E_{ads} is the average adsorption energy per CO molecule.

The critical first step in the splitting process is the adoption of a metastable $Rh_2(CO)_3$ configuration 0.17 eV above the ground state. Here, one CO molecule is adsorbed at an adatom-like Rh and the other two reside at a displaced
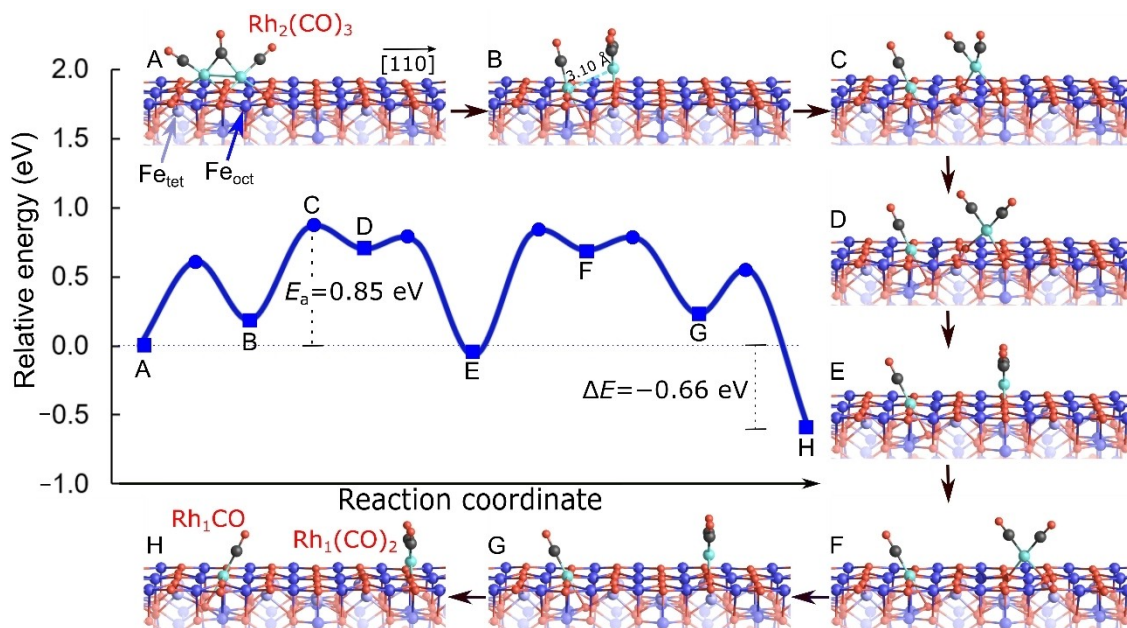
Figure 4. Proposed mechanism for $Rh_2(CO)_3$ splitting derived from DFT calculations. Configurations A and H represent the initial and final states of the splitting process, respectively, and are identical to the ground state structures depicted in Figure 3f and Figure 3g. Configurations B–G represent the intermediate steps along the reaction coordinate in the energy plot. The critical step (B) is the formation of a metastable $Rh_2(CO)_3$ configuration, in which the bridge CO molecule moves to occupy one of the Rh atoms. This induces a change in the Rh positions, and an elongation of the Rh–Rh distance to 3.10 Å. The remainder of the pathway involves the diffusion steps required for the $Rh_1(CO)_2$ to move and occupy an adatom-like site in a neighboring unit cell. The long diffusion process was split into multiple smaller CI-NEB calculations, each comprising three intermediate configurations. Surface Fe_{oct} atoms are dark blue, Fe_{tet} atoms are lighter and slate blue, as indicated by the two arrows in (a). Oxygen, carbon, and Rh atoms are red, black, and cyan, respectively.

Rh atom (configuration B in Figure 4). The Rh–Rh distance in this configuration is 3.10 Å, which is too long to be considered a bond. This suggests that the adsorption of 3 CO molecules will rapidly induce the breakup of the Rh_2 at room temperature, as observed in experiment. Configurations C to H show that the Rh_1CO remains in place after the initial split, consistent with the immobility of these species in the room-temperature STM movies. The $Rh_1(CO)_2$ species moves away along the [110] direction, aided by the close proximity of lattice oxygen atoms in this direction, ultimately arriving at another adatom-like 2-fold coordinated adsorption site in the neighboring unit cell, 11.8 Å away. Configurations E and G are the local minima along this path. These structures are somewhat similar to the configuration B, where the $Rh_1(CO)_2$ binds to two oxygen atoms above a subsurface Fe_{tet} atom. Configuration C represents the highest saddle point, which costs 0.85 eV. Finally. The most favorable configuration in configuration H has the $Rh_1(CO)$ and $Rh_1(CO)_2$ adsorbed in adatom-like sites in neighboring unit cells. In this final state, 0.66 eV is gained with respect to the initial $Rh_2(CO)_3$ configuration shown in configuration A.

On the basis of these calculations, we conclude that $Rh_2(CO)_3$ is the unstable intermediate that precedes the dimer splitting observed in STM. Finally, while the STM data shown in Figure 3 are representative, we note that not all Rh_2 dimers split to a monocarbonyl and a gem-dicarbonyl. In some instances, the post-breakup situation is

different (see Figure S3). For example, it is also possible to form a $Rh_1(CO)_2$ and a Rh atom incorporated in the surface layer, which displaces a surface Fe into a subsurface vacancy. We consider it likely that this process occurs when the dimer is in close proximity to $Fe_3O_4(001)$ surface defects.

The experimental and theoretical results described here align with the view that the behaviour of "single-atom" catalysts can be understood by analogy to coordination complexes. In this view, the metal–support bonds are ligands, and coordination vacancies are required in order to bind reactants. The as-deposited Rh atom is 2-fold coordinated to lattice oxygen atoms on $Fe_3O_4(001)$, which can be seen as a linear configuration, or as a square planar Rh complex with two coordination vacancies. The Bader charge of $+0.71\,e$ suggests a $+1$ charge state, which is typical for square planar Rh(I) complexes.[12] The presence of two coordination vacancies is an unstable situation, and one would expect this atom to be highly reactive for the adsorption of molecules from the gas phase such as CO.

Our STM and DFT data clearly show that a single CO molecule binds strongly (-2.57 eV), but it also causes the Rh atom to relax towards the support and create a pseudo-square planar environment utilizing a subsurface lattice O atom. This observation contrasts to prior work where CO was seen to destabilize Pt and Pd atoms on $Fe_3O_4(001)$,[13] but is explained by the oxophilicity of Rh, the presence of the subsurface O atoms in suitable locations, and the energetic gain that comes from completing the square planar

environment for the Rh. The rigidity of the surrounding lattice prevents the Rh atom moving even further down, and the subsurface O atom in question is already 4-fold coordinated to Fe. The resulting Rh–O bond (calculated bond length of 2.27 Å) is thus weak, and the system is able to flip between two symmetrically equivalent configurations at room temperature, as shown in Figure 1e and Movie S1. Imaging of the superposition of these states explains the elongated protrusion observed in STM. No further change to the Rh_1CO species was observed in any of our experiments, even though our DFT calculations suggest that binding a second CO molecule to create the gem-dicarbonyl should gain an additional -1.84 eV (Figure 1d and 1g). We note that spectroscopic identification of the Rh_1CO by CO infrared reflection absorption spectroscopy (IRAS) would be desirable, but is currently precluded by the poor sensitivity of IRAS on a Fe_3O_4 sample and the low density of Rh atoms on the surface.

Direct adsorption of a second CO molecule at the Rh_1 monocarbonyl is most likely prevented by steric hindrance. The ground state Rh_1CO configuration has the Rh atom essentially in the surface plane, with a CO molecule protruding, which makes it difficult for a second CO molecule to approach close enough to form a chemical bond. Consequently, formation of a Rh gem-dicarbonyl likely requires thermal excitation of the system into a metastable transition state in which it could accept a second CO molecule. Our DFT calculations find that the configuration shown in Figure S7b, which is essentially the Rh gem-dicarbonyl shown in Figure 1g with one missing CO molecule, is a local minimum located ≈ 0.5 eV higher in energy than the ground state. With this energy difference, the Rh_1CO spends a negligible fraction of time ($<10^{-8}$) in the metastable state at room temperature, and it is very unlikely to occur exactly when a CO molecule approaches. If the CO pressure were to be increased by many orders of magnitude, as it is in the CO titration experiments typically performed to characterize powder-based SAC samples, the probability to form dicarbonyls directly at the 2-fold coordinated Rh_1 site would be greatly enhanced. Once formed, the dicarbonyl would be stable due to the favourable thermodynamics, and measurable by IR spectroscopy. We have also considered another case where surface iron atoms are replaced by the Rh atoms, resulting in 5-fold coordinated Rh sites.[9b] As shown in Figure S8, the adsorption energy of CO on 5-fold coordinated Rh is -1.99 eV, which is significantly weaker than at the 2-fold coordinated Rh site. Dicarbonyl formation is not favourable at the 5-fold coordinated Rh atom: DFT calculations initiated in such a geometry always resulted in the second CO molecule moving to occupy a neighbouring surface Fe atom. This is straightforward to understand, because a monocarbonyl at the 5-fold Rh site produces a Rh atom with a complete octahedral coordination, which is common in coordination complexes. A dicarbonyl would see the Rh atom have seven ligands, which is not favourable. As such, we conclude that the dicarbonyl species commonly observed in CO titration experiments are not due to single atoms residing in highly coordinated substitutional sites.

The data shown in Figure 3 clearly demonstrate that if a $Rh_1(CO)_2$ species is formed, then it is stable at room temperature. The main reason the Rh_2 is able to form the dicarbonyl is because it can adsorb 3 CO molecules, which causes the split. When two molecules are adsorbed, our DFT calculations show that multiple configurations are accessible (Figure S5), but the one featuring a single CO at each Rh atom (Figure 3e) is the most favourable. This allows a third CO to adsorb in a bridge coordination, which weakens the Rh–Rh bond. Thereafter, the $Rh_2(CO)_3$ can take a second configuration in which the third CO binds to one of the Rh atoms forming a $Rh_1(CO)_2$. This splits off and diffuses to a nearby stable site, as shown in Movie S4 and Figure 4. This line of reasoning is supported by the fact that the Rh_1CO usually resides at the former position of the Rh_2, while the $Rh_1(CO)_2$ is located 11.8 Å along the direction of the Fe rows, occupying an equivalent adsorption site in the neighbouring unit cell (compare Figures 3a and 3c). The presence of the bridge adsorption site on $Rh_2(CO)_2$ is crucial for the breakup of the dimers because it increases the capacity of CO molecules that can be adsorbed to a number higher than one per Rh atom. We note that the presence of CO adsorbed in a bridge site is also a distinctive characteristic used in infrared spectroscopy to differentiate single-atom catalysts from particle catalysts.[14]

The atomic-scale insights obtained here rely on the combination of STM and DFT calculations. Considering the low surface concentrations of the Rh_2 dimer and $Rh_1(CO)_2$ dicarbonyl species involved, it is evident that this is not a suitable system for area-averaged spectroscopic techniques. It is important to recognize, however, that it is the precisely defined single crystal support and UHV environment that facilitate the direct comparison between experiment and theory. DFT calculations based on periodic boundary conditions are the computational analogue to single crystal-based studies, and the ability to adsorb molecules individually (in the absence of undefined contaminants) cannot be replicated in ambient-pressure experiments. The final benefit, which we exploit here, is the ability to follow adsorption events atom by atom in time-lapse movies in a reactive environment. Studying the dynamic evolution of the system using STEM is extremely challenging as it is difficult to continuously maintain atomic resolution, and long-time exposure to high energy electrons can significantly affect the system under study.[15] This was highlighted in a recent study by Yan et al.,[16] who demonstrated that Pt_2 dimers could split into two isolated Pt_1 single atoms by the electron beam during STEM measurements. It could be difficult to distinguish this from an adsorbate performing a similar role, as observed in the present work. In any case, our study demonstrates that atomically resolved STM is an ideal technique to study the stability and structural evolution of single-atom catalysts. It is also possible to visualize reaction mechanisms, as recently demonstrated by Guo et al., who reported an in situ visualization of ethylene polymerization on a carburized iron model catalyst and were able to image almost the entire sequence of the growth processes.[17]

Finally, we compare our results to those obtained for other metal atoms on $Fe_3O_4(001)$, and to the SAC literature

in general. We have previously shown that CO adsorption leads to the sintering of the $Pt_1/Fe_3O_4(001)$ and Pd_1/Fe_3O_4-(001) systems, which we attributed to the fact that these metals interact more strongly with CO than the metal oxide.[13] Interestingly, the CO-induced sintering of Pt led to $Pt_2(CO)_2$ species that were extremely stable, and only broke apart once the system was heated to 550 K and CO began to react with the $Fe_3O_4(001)$ support. The results for Rh described here are more in line with the $Ir/Fe_3O_4(001)$ system,[11] where a similar pseudo-square planar monocarbonyl structure was proposed. A limited number of $Ir_1(CO)_2$ gem-dicarbonyls were also observed in ref. [11] and it seems likely that the same dimer splitting mechanism was responsible. The breakup of small clusters by water exposure is also the basis for the "atom trapping" approach to forming stable SACs.[4,18] Moreover, it represents a way to recover the active state of the catalyst after thermal sintering, in a process termed "redispersion" in the SAC literature.[19] Interestingly, the detachment of carbonyl species from larger clusters has even been predicted to occur for metals with weak affinity to CO, such as Au.[20] Together, this all highlights the danger of assigning active species on the basis of as-prepared or post-mortem catalysts, the importance of further developing in situ and operando methods to study catalyst structure, and the important role that minority species invisible to area-averaging spectroscopies can play in single-atom catalysis.

Conclusions

A combination of STM movies and DFT calculations were used to study CO adsorption on Rh_1 and Rh_2 species on $Fe_3O_4(001)$. CO adsorption at Rh_1 species results in stable Rh_1CO monocarbonyls with a pseudo-square planar Rh coordination similar to that found in Rh(I) complexes. Square planar $Rh_1(CO)_2$ gem-dicarbonyls are also observed, but these come about exclusively through the CO-induced breakup of Rh_2 minority species. Our results clearly show that the adsorption of reactants can have a strong influence on the structure of the system, and that CO exposure can be used to redisperse small clusters that form during reactions. Overall, this work provides new insights into the rational design of superior SAC through the synthesis of dimer catalysts.

Acknowledgements

Conflict of Interest

The authors declare no conflict of interest.

Data Availability Statement

The data that support the findings of this study are available from the corresponding author upon reasonable request.

[1] a) S. K. Kaiser, Z. P. Chen, D. F. Akl, S. Mitchell, J. Perez-Ramirez, *Chem. Rev.* **2020**, *120*, 11703–11809; b) A. Wang, J. Li, T. Zhang, *Nat. Chem. Rev.* **2018**, *2*, 65–81; c) X. F. Yang, A. Q. Wang, B. T. Qiao, J. Li, J. Y. Liu, T. Zhang, *Accounts Chem Res* **2013**, *46*, 1740–1748.

[2] a) L. Nie, D. Mei, H. Xiong, B. Peng, Z. Ren, X. I. P. Hernandez, A. DeLaRiva, M. Wang, M. H. Engelhard, L. Kovarik, *Science* **2017**, *358*, 1419–1423; b) M. Moses-DeBusk, M. Yoon, L. F. Allard, D. R. Mullins, Z. Wu, X. Yang, G. Veith, G. M. Stocks, C. K. Narula, *J. Am. Chem. Soc.* **2013**, *135*, 12634–12645.

[3] a) F. Li, Y. Li, X. C. Zeng, Z. Chen, *ACS Catal.* **2015**, *5*, 544–552; b) H. Xu, C.-Q. Xu, D. Cheng, J. Li, *Catalysis Science, Technology* **2017**, *7*, 5860–5871.

[4] J. Jones, H. Xiong, A. T. DeLaRiva, E. J. Peterson, H. Pham, S. R. Challa, G. Qi, S. Oh, M. H. Wiebenga, X. I. Pereira Hernández, *Science* **2016**, *353*, 150–154.

[5] a) K. Ding, A. Gulec, A. M. Johnson, N. M. Schweitzer, G. D. Stucky, L. D. Marks, P. C. Stair, *Science* **2015**, *350*, 189–192; b) C. Dessal, T. Len, F. Morfin, J.-L. Rousset, M. Aouine, P. Afanasiev, L. Piccolo, *ACS Catal.* **2019**, *9*, 5752–5759.

[6] a) I. Ro, J. Qi, S. Lee, M. Xu, X. Yan, Z. Xie, G. Zakem, A. Morales, J. G. Chen, X. Pan, *Nature* **2022**, *609*, 287–292; b) R. Lang, T. Li, D. Matsumura, S. Miao, Y. Ren, Y. T. Cui, Y. Tan, B. Qiao, L. Li, A. Wang, *Angew. Chem. Int. Ed.* **2016**, *55*, 16054–16058; c) M. G. Farpón, W. Henao, P. N. Plessow, E. Andrés, R. Arenal, C. Marini, G. Agostini, F. Studt, G. Prieto, *Angew. Chem.* **2023**, *135*, e202214048; d) L. Wang, W. Zhang, S. Wang, Z. Gao, Z. Luo, X. Wang, R. Zeng, A. Li, H. Li, M. Wang, X. Zheng, J. Zhu, W. Zhang, C. Ma, R. Si, J. Zeng, *Nat. Commun.* **2016**, *7*, 14036; e) J. Amsler, B. B. Sarma, G. Agostini, G. Prieto, P. N. Plessow, F. Studt, *J. Am. Chem. Soc.* **2020**, *142*, 5087–5096; f) I. Ro, M. Xu, G. W. Graham, X. Pan, P. Christopher, *ACS Catal.* **2019**, *9*, 10899–10912.

[7] R. Bliem, E. McDermott, P. Ferstl, M. Setvin, O. Gamba, J. Pavelec, M. Schneider, M. Schmid, U. Diebold, P. Blaha, *Science* **2014**, *346*, 1215–1218.

[8] B. Arndt, R. Bliem, O. Gamba, J. E. S. van der Hoeven, H. Noei, U. Diebold, G. S. Parkinson, A. Stierle, *Surf. Sci.* **2016**, *653*, 76–81.

[9] a) J. Hulva, M. Meier, R. Bliem, Z. Jakub, F. Kraushofer, M. Schmid, U. Diebold, C. Franchini, G. S. Parkinson, *Science* **2021**, *371*, 375–379; b) Z. Jakub, J. Hulva, P. T. Ryan, D. A. Duncan, D. J. Payne, R. Bliem, M. Ulreich, P. Hofegger, F. Kraushofer, M. Meier, *Nanoscale* **2020**, *12*, 5866–5875.

[10] R. Bliem, J. Pavelec, O. Gamba, E. McDermott, Z. Wang, S. Gerhold, M. Wagner, J. Osiecki, K. Schulte, M. Schmid, *Phys. Rev. B* **2015**, *92*, 075440.

[11] Z. Jakub, J. Hulva, M. Meier, R. Bliem, F. Kraushofer, M. Setvin, M. Schmid, U. Diebold, C. Franchini, G. S. Parkinson, *Angew. Chem. Int. Ed.* **2019**, *58*, 13961–13968.

[12] a) P. Meakin, J. Jesson, C. Tolman, *J. Am. Chem. Soc.* **1972**, *94*, 3240–3242; b) J. A. Osborn, F. H. Jardine, J. F. Young, G. Wilkinson, *J. Chem. Soc. A* **1966**, 1711–1732.

[13] a) G. S. Parkinson, Z. Novotny, G. Argentero, M. Schmid, J. Pavelec, R. Kosak, P. Blaha, U. Diebold, *Nat. Mater.* **2013**, *12*, 724–728; b) M. Meier, J. Hulva, Z. Jakub, F. Kraushofer, M. Bobić, R. Bliem, M. Setvin, M. Schmid, U. Diebold, C. Franchini, *Sci. Adv.* **2022**, *8*, eabn4580.

[14] a) B. Qiao, A. Wang, X. Yang, L. F. Allard, Z. Jiang, Y. Cui, J. Liu, J. Li, T. Zhang, *Nat. Chem.* **2011**, *3*, 634–641; b) M. Kottwitz, Y. Li, H. Wang, A. I. Frenkel, R. G. Nuzzo, *Chemistry-Methods* **2021**, *1*, 278–294.

[15] a) Q. L. Chen, C. Dwyer, G. Sheng, C. Z. Zhu, X. N. Li, C. L. Zheng, Y. H. Zhu, *Adv. Mater.* **2020**, *32*, 1907619; b) X. Tang, J. Ye, L. Guo, T. Pu, L. Cheng, X. M. Cao, Y. Guo, L. Wang, Y. Guo, W. Zhan, *Adv. Mater.* **2023**, *35*, 2208504.

[16] H. Yan, Y. Lin, H. Wu, W. H. Zhang, Z. H. Sun, H. Cheng, W. Liu, C. L. Wang, J. J. Li, X. H. Huang, T. Yao, J. L. Yang, S. Q. Wei, J. L. Lu, *Nat. Commun.* **2017**, *8*, 1070.

[17] W. Guo, J. Yin, Z. Xu, W. Li, Z. Peng, C. Weststrate, X. Yu, Y. He, Z. Cao, X. Wen, *Science* **2022**, *375*, 1188–1191.

[18] A. Datye, Y. Wang, *Natl. Sci. Rev.* **2018**, *5*, 630–632.

[19] a) H. Jeong, G. Lee, B.-S. Kim, J. Bae, J. W. Han, H. Lee, *J. Am. Chem. Soc.* **2018**, *140*, 9558–9565; b) M. Farnesi Camellone, F. Dvořák, M. Vorokhta, A. Tovt, I. Khalakhan, V. Johánek, T. Skála, I. Matolínová, S. Fabris, J. Mysliveček, *ACS Catal.* **2022**, *12*, 4859–4871; c) Q. Wan, F. Wei, Y. Wang, F. Wang, L. Zhou, S. Lin, D. Xie, H. Guo, *Nanoscale* **2018**, *10*, 17893–17901; d) K. Liu, X. Zhao, G. Ren, T. Yang, Y. Ren, A. F. Lee, Y. Su, X. Pan, J. Zhang, Z. Chen, J. Yang, X. Liu, T. Zhou, W. Xi, J. Luo, C. Zeng, H. Matsumoto, W. Liu, Q. Jiang, K. Wilson, A. Wang, B. Qiao, W. Li, T. Zhang, *Nat. Commun.* **2020**, *11*, 1263.

[20] Y.-G. Wang, D. C. Cantu, M.-S. Lee, J. Li, V.-A. Glezakou, R. Rousseau, *J. Am. Chem. Soc.* **2016**, *138*, 10467–10476.